Journal of Power Sources 240 (2013) 178–183

Contents lists available at SciVerse ScienceDirect

Journal of Power Sources

journal homepage: www.elsevier.com/locate/jpowsour

Microstructures and electrochemical hydrogen storage characteristics of $La_{0.7}Ce_{0.3}Ni_{4.2}Mn_{0.9-x}Cu_{0.37}(Fe_{0.43}B_{0.57})_x$ ($x = 0$–0.20) alloys

Xianyun Peng [a], Baozhong Liu [a,*], Yanping Fan [a], Xilin Zhu [c], Qiuming Peng [b,*], Zhi Zhang [a]

[a] School of Materials Science & Engineering, Henan Polytechnic University, No. 2001, Century Avenue, Jiaozuo 454000, China
[b] State Key Laboratory of Metastable Materials Science and Technology, Yanshan University, Qinhuangdao 066004, China
[c] Inner Mongolia Rare Earth Ovonic Metal Hydride Co. Ltd., Baotou 014030, China

HIGHLIGHTS

- Commercial $Fe_{0.43}B_{0.57}$ is much cheaper than B and has lower melting point than B.
- Alloys containing $Fe_{0.43}B_{0.57}$ consist of $LaNi_5$ phase and $La_3Ni_{13}B_2$ phase.
- Activation property is improved by increasing $Fe_{0.43}B_{0.57}$ content.
- The alloy with $x = 0.10$ exhibits the best HRD.
- C_{max} and cycling stability decrease with increasing x value.

ARTICLE INFO

Article history:
Received 15 February 2013
Received in revised form
1 April 2013
Accepted 2 April 2013
Available online 9 April 2013

Keywords:
Alloys
X-ray diffraction
Microstructures
Electrochemical properties
Nickel/metal hydride battery

ABSTRACT

Microstructures and electrochemical characteristics of $La_{0.7}Ce_{0.3}Ni_{4.2}Mn_{0.9-x}Cu_{0.37}(Fe_{0.43}B_{0.57})_x$ ($x = 0$–0.20) hydrogen storage alloys are investigated. X-ray diffraction and backscattered electron results indicate that the pristine alloy is single $LaNi_5$ phase while the alloys containing $Fe_{0.43}B_{0.57}$ consist of $LaNi_5$ matrix phase and $La_3Ni_{13}B_2$ secondary phase. The relative abundance of $La_3Ni_{13}B_2$ phase increases with the increase in x value. The a and V of $LaNi_5$ phase increase with increasing x value. Activation property of the alloy electrodes is improved by substituting Mn with $Fe_{0.43}B_{0.57}$. Maximum discharge capacity of the alloy electrodes monotonically decreases from 323.3 mAh g^{-1} ($x = 0$) to 311.3 mAh g^{-1} ($x = 0.20$). Cycling capacity retention rate at the 100th cycle decreases from 79.3% ($x = 0$) to 68.2% ($x = 0.20$) with increasing x value, which is ascribed to the degradation of corrosion resistance. High-rate dischargeability of the alloy electrodes first increases with increasing x from 0 to 0.10, and then decreases until x increases to 0.20. It demonstrates that the substitution of Mn with $Fe_{0.43}B_{0.57}$ is an effective approach to improve the overall electrochemical performances of the Co-free high-Mn alloy electrodes.

1. Introduction

Recently, nickel/metal hydride (Ni/MH) secondary batteries have been adopted in various portable electronic devices because of their good electrochemical performance and environment compatibility. Almost all of the commercial Ni/MH batteries are employing AB_5-type alloys as negative electrode materials due to their good overall electrode properties [1,2]. However, high cost of AB_5-type alloys slows down the rhythms of wide applications. Substantial efforts have been dedicated to reduce their costs by eliminating Nd and Pr [3] or substituting Co with foreign metals, such as, Mn, Fe, Cu, Si, etc [4–7]. Thereafter, the Co-free high-Mn alloys were developed and commercially produced [8]. However, the electrochemical performances, especially high-rate dischargeability, of Co-free high-Mn alloys are not yet satisfying. Thus, it is necessary to further improve the electrochemical hydrogen storage properties without increasing their expenses. It is difficult to further decrease the cost by modifying composition of A site in Co-free AB_5 type alloy because A site elements are usually La or La and Ce, whose raw materials are pure La and La/Ce mischmetal [9–11]. However, pure Mn, Ni and Cu are used as raw materials for B site element. It is possible to reduce the raw cost and to modify the electrochemical hydrogen storage properties by substituting B site element with the alloys, such as, FeB, FeV, MoFe, etc., whose cost is lower compared with pure Mn, Ni or Cu.

Yang et al. [12] found that the substitution of B for Ni in $MmNi_{3.70-x}Mn_{0.35}Co_{0.60}Al_{0.25}B_x$ hydrogen storage alloys improved

* Corresponding authors. Tel./fax: +86 391 3989859.
E-mail addresses: bzliu@hpu.edu.cn, b_z_liu@163.com (B. Liu), pengqiuming@gmail.com (Q. Peng).

0378-7753/$ – see front matter © 2013 Elsevier B.V. All rights reserved.
http://dx.doi.org/10.1016/j.jpowsour.2013.04.004

the activation ability and the high-rate dischargeability of the alloy electrodes. Ye et al. [13] reported that the addition of B modified the activation performance and significantly improved the high-rate capacity of $Mm_{3.55}Co_{0.75}Mn_{0.4}Al_{0.3}B_x$ alloy though the electrochemical capacity was lower than that of commercial $Mm_{3.55}Co_{0.75}Mn_{0.4}Al_{0.3}$ alloy. Zhang et al. [14] pointed out that the addition of B improved the cycling stability, high rate discharge capability and discharge voltage for $MmNi_{3.8}Co_{0.4}Mn_{0.6}Al_{0.2}B_x$ alloys. Obviously, the addition of B element is effective to enhance activation performance and high-rate dischargeability. However, the pure B is very expensive and unpractical to be used in the Co-less or Co-free alloy. Fortunately, the price of commercial $Fe_{0.43}B_{0.57}$ alloy is less than 5% price of pure B, and the melt point of $Fe_{0.43}B_{0.57}$ alloy is much lower compared with pure B and the lower melt point of $Fe_{0.43}B_{0.57}$ alloy facilitates the homogeneity of the alloy. More importantly, it is reported that Fe introduction in AB_5 alloy can remarkably improve cycling stability due to the improvement in the anti-pulverization of the alloy electrode [15,16]. Therefore, it can be expected that the overall electrochemical characteristics could be improved by substituting of $Fe_{0.43}B_{0.57}$ alloy for Mn in Co-free high-Mn AB_5-type alloys.

Ye et al. [17] have reported that Fe–B can replace B as additive in $MmNi_{3.55}Co_{0.75}Mn_{0.4}Al_{0.3}B_{0.3}$ alloy without the significant decrease of high-rate dischargeabiltiy. Moreover, it has been proven that $Fe_{0.43}B_{0.57}$ is successfully used to substitute Ni, Cu or Co instead of pure B and Fe in Co-less and Co-free AB_5 type alloys in our previous investigations [18–20]. Thus, it is feasible and promising to substitute Mn with $Fe_{0.43}B_{0.57}$ in Co-free high-Mn alloy. Here, on the basis of the merits of $Fe_{0.43}B_{0.57}$ and the belief that the Fe and B additions may result in some noticeable modifications of electrochemical hydrogen storage performance, microstructures and electrochemical hydrogen storage characteristics of $LaNi_{3.55}Co_{0.2-x}Mn_{0.35}Al_{0.15}Cu_{0.75}(Fe_{0.43}B_{0.57})_x$ (x = 0–0.20) alloys have been investigated.

2. Experimental procedures

$La_{0.7}Ce_{0.3}Ni_{4.2}Mn_{0.9-x}Cu_{0.37}(Fe_{0.43}B_{0.57})_x$ (x = 0–0.20) alloys were synthesized by induction melting of the metal elements (La, Ce, Ni, Mn, Al, Cu: 99.9% in purity and commercial Fe–B alloy contained 57.0 at.% B and the other were Fe and trace impurities.) in argon atmosphere. The ingots were annealed by using vacuum heat-treating furnace. Before heating, the sample cell was vacuumized until pressure is less than 10 Pa and then the argon was charged into the sample cell until the pressure was 0.8 MPa. The samples were heated from room temperature to 1223 K at the rate of 10 K min^{-1} and then kept in 1223 K for 2 h followed by natural cooling in the furnace.

X-ray diffraction (XRD) measurement was carried out on X'pert PROMPD X-ray diffractometer with Cu Kα radiation in the range from 20° to 85° with 0.02° min^{-1}, and the results were analyzed by means of Rietveld refinement (using the software MAUD). Back-scattered electron (BSE) images were obtained by using HITACHI-4800 scanning electron microscope with an energy dispersive X-ray spectrometer (EDS). The hydrogen storage properties of the alloys were studied by using pressure–composition–temperature (PCT) (made by Suzuki Shokan in Japan) at 314 K. Before the PCT measurement, the alloys were activated by 5 hydriding/dehydriding cycles. The delay time was 180 s and maximum pressure was 2 MPa.

The alloy powders of measuring electrodes were obtained by grinding the inner part of alloy ingots in the Ar atmosphere. All measuring electrodes for test were prepared by cold pressing the mixture of 0.15 g alloy powders of 200–400 mesh and 0.75 g nickel carbonyl powders into a pellet of 10 mm in diameter under 15 MPa. Electrochemical measurements were performed at 298 K in a standard tri-electrode system, consisting of a working electrode (metal hydride), a counter electrode ($Ni(OH)_2$/NiOOH), and a reference electrode (Hg/HgO) with 6 mol L^{-1} KOH solution as electrolyte. Each electrode was charged for 7 h at 60 mA g^{-1} and discharged to −0.6 V versus Hg/HgO at 60 mA g^{-1} at 298 K. After every charging/discharging, the rest time was 10 min. In evaluating the high-rate dischargeability, discharge capacity of the alloy electrodes at different discharge current density was measured. The high-rate dischargeability (HRD, %) was defined as

$$HRD = C_d/C_{max} \times 100\% \quad (1)$$

where C_d was the discharge capacity at the discharge current density I_d (I_d = 60, 300, 600, 900 and 1200 mA g^{-1}, respectively), and C_{max} was the maximum discharge capacity at the discharge current density of 60 mA g^{-1}.

The linear polarization curves were performed on a PARSTAT 2273 Advanced Potentiostat/Galvanostat station (using linear polarization in the PowerCORR software) by scanning the electrode potential at the rate of 0.1 mV s^{-1} from −5 to 5 mV (versus open circuit potential) at 50% depth of discharge (DOD) at 298 K. The potential step measurements were tested on the same instrument (using potentiostatic in the PowerCORR software) at 100% charge state. A +500 mV potential was applied and the discharge time was 3600 s.

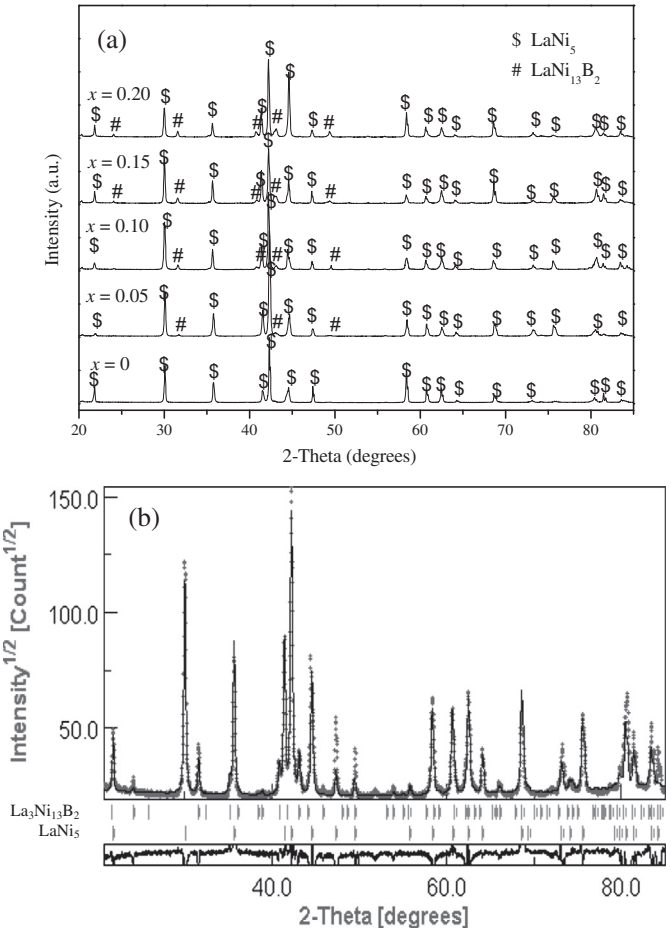

Fig. 1. XRD patterns of $La_{0.7}Ce_{0.3}Ni_{4.2}Mn_{0.9-x}Cu_{0.37}(Fe_{0.43}B_{0.57})_x$ alloys, (a) XRD patterns for x = 0–0.20, (b) Rietveld analysis pattern for x = 0.10.

Table 1
The characteristics of phases in $La_{0.7}Ce_{0.3}Ni_{4.2}Mn_{0.9-x}Cu_{0.37}(Fe_{0.43}B_{0.57})_x$ alloys.

Samples	Phases	Lattice parameter (Å)		Cell volume (Å^3)	Phase abundance (%)
$x = 0$	$LaNi_5$	$a = 5.0178$	$c = 4.0564$	88.45	100
$x = 0.05$	$LaNi_5$	$a = 5.0238$	$c = 4.0588$	88.71	97.43
	$La_3Ni_{13}B_2$	$a = 5.1247$	$c = 10.9734$		2.67
$x = 0.10$	$LaNi_5$	$a = 5.0270$	$c = 4.0607$	88.87	91.72
	$La_3Ni_{13}B_2$	$a = 5.1141$	$c = 10.9910$		8.28
$x = 0.15$	$LaNi_5$	$a = 5.0287$	$c = 4.0615$	88.94	88.84
	$La_3Ni_{13}B_2$	$a = 5.1027$	$c = 11.0281$		11.26
$x = 0.20$	$LaNi_5$	$a = 5.0311$	$c = 4.0620$	89.04	84.76
	$La_3Ni_{13}B_2$	$a = 5.0998$	$c = 11.0637$		15.24

3. Results and discussion

3.1. Crystal structure

Fig. 1a presents XRD patterns of $La_{0.7}Ce_{0.3}Ni_{4.2}Mn_{0.9-x}Cu_{0.37}(Fe_{0.43}B_{0.57})_x$ alloys. Fig. 1b shows the XRD pattern and Rietveld analysis pattern of $La_{0.7}Ce_{0.3}Ni_{4.2}Mn_{0.8}Cu_{0.37}(Fe_{0.43}B_{0.57})_{0.1}$ alloy. Lattice parameters, cell volume and phase relative abundance of the alloys are listed in Table 1. $La_{0.7}Ce_{0.3}Ni_{4.2}Mn_{0.9}Cu_{0.37}$ alloy is single $LaNi_5$ phase with $CaCu_5$ type hexagonal structure. The alloys containing $Fe_{0.43}B_{0.57}$ are composed of $LaNi_5$ matrix phase and $La_3Ni_{13}B_2$ secondary phase. The relative abundance of $La_3Ni_{13}B_2$ phase increases, and the a and V of $LaNi_5$ phase increase with increasing x value.

Fig. 2a shows BSE image of $La_{0.7}Ce_{0.3}Ni_{4.2}Mn_{0.7}Cu_{0.37}(Fe_{0.43}B_{0.57})_{0.2}$ alloy, where the $La_{0.7}Ce_{0.3}Ni_{4.2}Mn_{0.7}Cu_{0.37}(Fe_{0.43}B_{0.57})_{0.2}$ alloy consists of matrix phase (shallow black region) and secondary phase (white gray region). Fig. 2b shows EDS result of shallow black region in $La_{0.7}Ce_{0.3}Ni_{4.2}Mn_{0.7}Cu_{0.37}(Fe_{0.43}B_{0.57})_{0.2}$ alloy. The shallow black region is $LaNi_5$ matrix phase. According to XRD result, it is reasonable to believe that the white gray region is $La_3Ni_{13}B_2$ secondary phase.

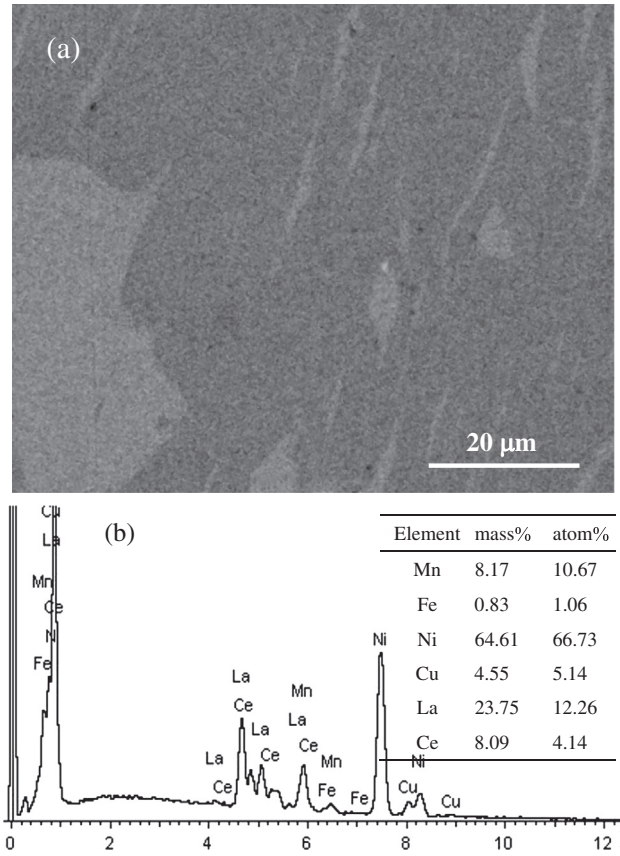

Fig. 2. BSE and EDS result of $La_{0.7}Ce_{0.3}Ni_{4.2}Mn_{0.7}Cu_{0.37}(Fe_{0.43}B_{0.57})_{0.2}$ alloy, (a) BSE, (b) EDS result of shallow black regions.

Table 2
Electrochemical properties of $La_{0.7}Ce_{0.3}Ni_{4.2}Mn_{0.9-x}Cu_{0.37}(Fe_{0.43}B_{0.57})_x$ alloy electrodes.

x	C_{max} (mAh g^{-1})	N_a[b]	HRD_{1200}[a] (%)	S_{100} (%)
0	323.3	5	60.1	79.3
0.05	316.8	4	64.3	77.6
0.10	316.3	3	69.8	74.5
0.15	313.7	3	66.1	71.0
0.20	311.3	2	63.2	68.2

[a] The high-rate dischargeability at the discharge current density of 1200 mA g^{-1}.
[b] The number of cycles needed to activate the electrode.

3.2. Activation capability and maximum discharge capability

The number of cycles (N_a) needed to activate the electrodes and maximum discharge capacity (C_{max}) of $La_{0.7}Ce_{0.3}Ni_{4.2}Mn_{0.9-x}Cu_{0.37}(Fe_{0.43}B_{0.57})_x$ alloy electrodes are given in Table 2. It is noted that the N_a of the alloy electrodes decreases from 5 ($x = 0$) to 2 ($x = 0.20$) with increasing x value, which indicates that the substitution of Mn by $Fe_{0.43}B_{0.57}$ significantly improves the activation performance. Shu et al. [21] pointed out that the phase interface or grain boundary contributed to the activation of alloy electrode because the interface or boundary was a buffer area of the releasing of the lattice stress and strain energy. In our results, the relative abundance of $La_3Ni_{13}B_2$ secondary phase increases with the increment of x value. It causes the increase in volume fraction of phase boundary correspondingly, which decreases the lattice distortion and strain energy formed in the process of hydrogen absorption, and then contributes to the activation property. In addition, it is believed that the electrocatalytic activity of the alloy surface contributed to the rapid activation [22,23]. B can effectively improve the surface electrocatalytic activity of alloy surface [12]. With increasing x value, the increase in B content gives rise to the electrochemical activity of alloy surface, and therefore improves the activation property. However, Wu et al. [24] reported the oxidation film formed on the alloy surface increased the additive internal energy, which led to the poorer activation performance. Due to the low surface energy of Fe, the increase in Fe content makes the surface oxide layer become thick and causes the increase in internal energy, and then degrades activation property. Thus, the advantageous factors are prominent for the improvement in activation performance of $La_{0.7}Ce_{0.3}Ni_{4.2}Mn_{0.9-x}Cu_{0.37}(Fe_{0.43}B_{0.57})_x$ alloy electrodes in present work.

The C_{max} of the alloy electrodes decreases monotonically from 323.3 mAh g^{-1} ($x = 0$) to 311.3 mAh g^{-1} ($x = 0.20$) with increasing x value. In general, maximum discharge capacity is related to the crystalline structure and electrochemical kinetics. The decrease in C_{max} of the alloy electrodes may be ascribed to the following factors. Firstly, the hydrogen storage capacity of $La_3Ni_{13}B_2$ phase is 157 mAh g^{-1} [25], which is much lower discharge capacity than that of $LaNi_5$ matrix phase. The $La_3Ni_{13}B_2$ secondary phase increases gradually with increasing amount of $Fe_{0.43}B_{0.57}$, which is unfavorable for the discharge capacity. Secondly, PCT curves of $La_{0.7}Ce_{0.3}Ni_{3.75-x}Mn_{0.35}Al_{0.15}Cu_{0.75}(V_{0.81}Fe_{0.19})_x$ alloys are showed in Fig. 3, it can seen that the hydrogen storage capacity of alloys decreases with increasing x value, which is detrimental to the maximum discharge capacity. Thirdly, the increase in Fe content leads to the surface oxide film thicker, which degrades the charge-transfer reaction on the alloy surface. The oxide film also decreases the number of activity sites on the alloy surface and then makes the diffusion of hydrogen from the inner to the surface more difficultly.

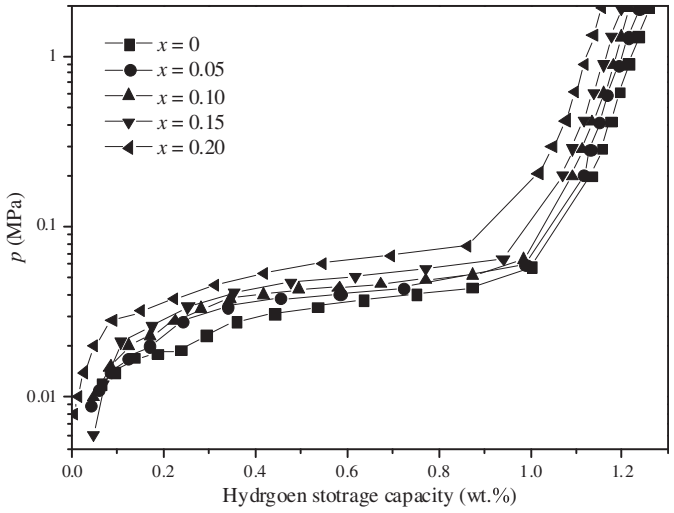

Fig. 3. PCT curves of $La_{0.7}Ce_{0.3}Ni_{4.2}Mn_{0.9-x}Cu_{0.37}(Fe_{0.43}B_{0.57})_x$ alloys.

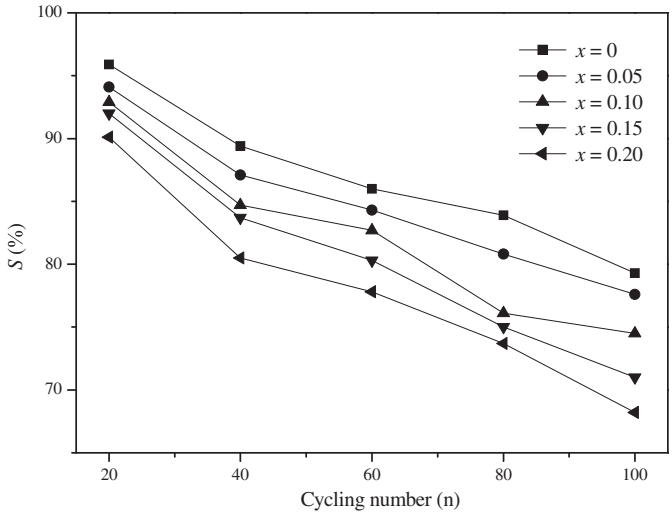

Fig. 4. Cycling stability of $La_{0.7}Ce_{0.3}Ni_{4.2}Mn_{0.9-x}Cu_{0.37}(Fe_{0.43}B_{0.57})_x$ alloy electrodes.

3.3. Cycling stability

Cycling stability is an extremely important factor for the service life of hydrogen storage alloys. The cycling capacity retention rate is expressed as S_n (%) = C_n/C_{max} × 100 (where C_n is the discharge capacity at the nth cycle). The cycling capacity retention rate of $La_{0.7}Ce_{0.3}Ni_{4.2}Mn_{0.9-x}Cu_{0.37}(Fe_{0.43}B_{0.57})_x$ alloy electrodes as a function of cycling number is shown in Fig. 4. Cycling stability decreases with increasing x from 0 to 0.20. The S_{100} of the alloy electrodes are listed in Table 2. It can be seen that S_{100} monotonically decreases from 79.3% ($x = 0$) to 68.2% ($x = 0.20$). The fundamental reasons for the capacity decay of alloy electrode are attributed to the pulverization and corrosion of the alloy in the charging–discharging cycle [26,27]. The formation of the secondary phase increases the number of phase boundary as buffer areas for the release of distortion and stress of crystal lattice in the charging/discharging process, and then restricted the pulverization [28]. The $La_3Ni_{13}B_2$ secondary phase increases the amount of phase boundary, which releases the stress formed in the process of hydrogen absorbing and then improves anti-pulverization of the alloy electrodes. On the other hand, it is well-known that Fe easily oxidized due to the lower surface energy and forms coarse oxide film. The increase in Fe content not only causes the deterioration of the corrosion resistance with increasing x value and then increases the loss of the alloy, but also degrades the electrochemical kinetics on the alloy surface, which is detrimental to the discharge capacity. Moreover, the coarse oxide film on the alloy surface cannot prevents the dissolution of Mn away easily from the alloy electrode into the electrolyte. In addition, Fig. 5 presents the Tafel curves of $La_{0.7}Ce_{0.3}Ni_{4.2}Mn_{0.9-x}Cu_{0.37}(Fe_{0.43}B_{0.57})_x$ alloy electrodes. Clearly the corrosion potential of alloy electrodes becomes more negative and the corrosion current increases with increasing x value, indicating the corrosion resistance of alloy electrodes decreases with increasing x value. Thus, it is reasonable to believe that the decrease in corrosion resistance of alloy electrode is one of critical reasons for the degradation of cycling stability in present work.

3.4. High-rate dischargeability and electrochemical kinetics

Fig. 6 shows the relationship between the high-rate dischargeability (HRD) and the discharge current density of $La_{0.7}Ce_{0.3}Ni_{4.2}Mn_{0.9-x}Cu_{0.37}(Fe_{0.43}B_{0.57})_x$ alloy electrodes. The HRD of the alloy electrodes first increases with increasing x from 0 to 0.10, and then decreases when x increases to 0.20. The HRD at the discharge current density of 1200 mA g^{-1} (HRD_{1200}) is listed in Table 2. It can be seen that HRD_{1200} first increases from 60.1% ($x = 0$) to 69.8% ($x = 0.10$), and then decreases to 63.2% ($x = 0.20$).

It is well known that the HRD of the metal-hydride electrodes is dominated by the charge-transfer reaction at the electrode/electrolyte interface and the hydrogen diffusion rate within the bulky alloy electrode, which are reflected in the value of surface exchange current density (I_0), being a measure of the catalytic activity of an alloy, as well as in the hydrogen diffusion coefficient (D), which characterizes the mass transport properties of an alloy electrode [29].

Fig. 7 shows the linear polarization curves of $La_{0.7}Ce_{0.3}Ni_{4.2}Mn_{0.9-x}Cu_{0.37}(Fe_{0.43}B_{0.57})_x$ alloy electrodes at 50% DOD and 298 K. The polarization resistances (R_p) is calculated through estimating the slopes of linear polarization curves, and listed in Table 3. The R_p values of the alloy electrodes first decreases from 208.2 mΩ g ($x = 0$) to 132.8 mΩ g ($x = 0.10$), and then increases to 171.4 mΩ g ($x = 0.20$) with increasing x value. Furthermore, the exchange current density I_0 can also describe the charge-transfer process. The I_0 value can be calculated according to the following formula [30].

$$I_0 = \frac{RT}{FR_p} \quad (2)$$

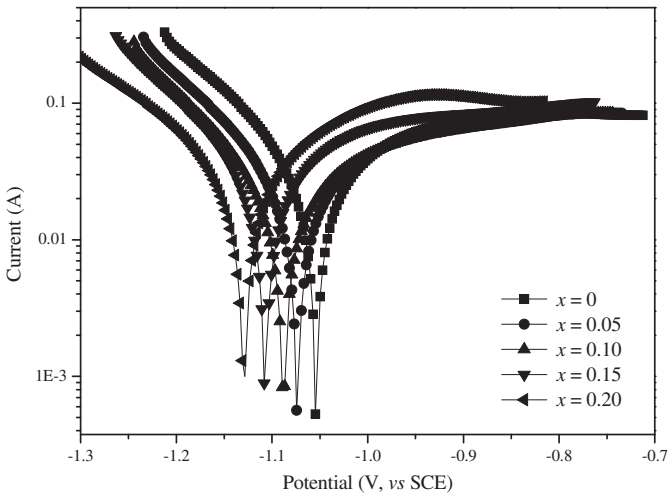

Fig. 5. Tafel curves of $La_{0.7}Ce_{0.3}Ni_{4.2}Mn_{0.9-x}Cu_{0.37}(Fe_{0.43}B_{0.57})_x$ alloy electrodes.

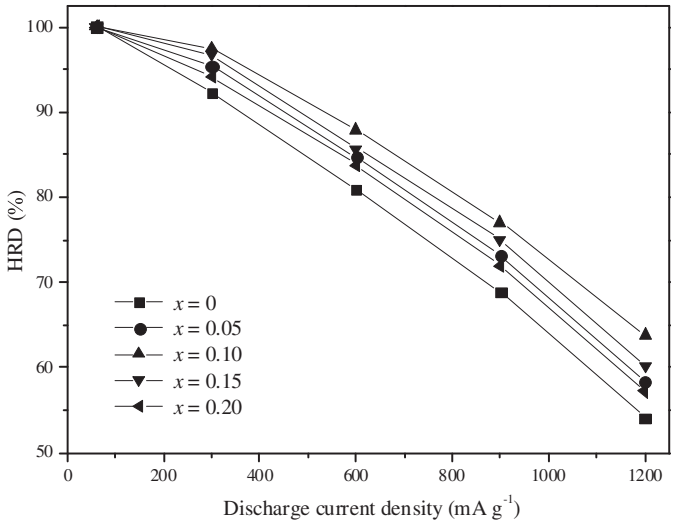

Fig. 6. HRD of $La_{0.7}Ce_{0.3}Ni_{4.2}Mn_{0.9-x}Cu_{0.37}(Fe_{0.43}B_{0.57})_x$ alloy electrodes.

where R, T, F, R_p are the gas constant, absolute temperature, Faraday constant and the polarization resistance, respectively. The I_0 values are calculated by Eq. (1) listed in Table 3. It is clear that the I_0 first increases from 123.3 mA g^{-1} ($x = 0$) to 193.4 mA g^{-1} ($x = 0.05$), and then decreases to 149.8 mA g^{-1} ($x = 0.20$). It is reported that the formation of the $La_3Ni_{13}B_2$ secondary phase in AB_5 alloys improves the catalytic activity of the alloys [20]. As mentioned above, the secondary phase $La_3Ni_{13}B_2$ increases with increasing x value, which is of benefit to improve the electrocatalytic activity of the surface of alloy electrode and the charge-transfer reaction. Unfortunately, the increase in Fe content on the alloy surface with increasing x value degrades the charge-transfer reaction because of the increase of oxide film on the alloy surface. Moreover, since Mn is very unstable in the alkaline electrolyte, so it will dissolve away easily from the electrode into the electrolyte and results in a microporous electrode surface with high specific area of nickel in the alloy surface layer and subsurface. The addition of Mn in AB_5 alloy will improve the electrocatalytic activity of alloy electrode [31,32]. The decrease of Mn with increasing x value is also detrimental to the charge transfer reaction. Therefore, it is reasonable to assume that, when $x \leq 0.10$, the favorable effect is chiefly responsible for the increase of the exchange current density for alloy electrodes. However, when

Table 3
Electrochemical kinetic characteristics of $La_{0.7}Ce_{0.3}Ni_{4.2}Mn_{0.9-x}Cu_{0.37}(Fe_{0.43}B_{0.57})_x$ alloy electrodes.

x	R_p (mΩ g)	I_0 (mA g^{-1})	D ($\times 10^{-11}$ cm^2 s^{-1})
0	208.2	123.3	6.28
0.05	163.0	157.5	6.63
0.10	132.8	193.4	9.42
0.15	147.5	174.1	8.51
0.20	171.4	149.8	7.70

$x > 0.10$, the decrease of the exchange current density for alloy electrodes is mainly ascribed to the disadvantageous factors. Consequently, the threshold content of $Fe_{0.43}B_{0.57}$ is 0.1 in present system.

Fig. 8 shows the semi-logarithmic plots of the anodic current vs. the time response of $La_{0.7}Ce_{0.3}Ni_{4.2}Mn_{0.9-x}Cu_{0.37}(Fe_{0.43}B_{0.57})_x$ alloy electrodes. It can be seen that the current–time responses can be divided into two time domains [33], in the first time region, the oxidation current of hydrogen rapidly declines due to the rapid consumption of hydrogen on the surface. However, in the followed second time region, the current declines more slowly and drops linearly with time. Since hydrogen is supplied from the bulk of the alloy at a rate proportional to the concentration gradient of hydrogen, hence the electrode current is controlled by the diffusion of hydrogen in the second time region. Zheng et al. [33] reported that in a large anodic potential-step test, after a long discharge time, the diffusion current varies with time according to the following equation:

$$\lg i = \lg\left(\frac{6FD}{da^2}(C_0 - C_s)\right) - \frac{\pi^2}{2.303}\frac{D}{a^2}t \quad (3)$$

where i is anodic current density (A g^{-1}), D the hydrogen diffusion coefficient (cm^2 s^{-1}), d the density of the alloy (g cm^{-3}), a the radius of the alloy particle, C_0 the initial hydrogen concentration in the bulk of the alloy (mol cm^{-3}), C_s the surface hydrogen concentration of the alloy (mol cm^{-3}) and t is the discharge time (s). Assuming that the alloy has a similar particle distribution with an average particle radius of 13 μm according to previous study [34], D was calculated and summarized in Table 3. The D of $La_{0.7}Ce_{0.3}Ni_{4.2}Mn_{0.9-x}Cu_{0.37}(Fe_{0.43}B_{0.57})_x$ alloy electrodes first increases from 6.28 × 10^{-11} ($x = 0$) to 9.42 × 10^{-11} cm^2 s^{-1} ($x = 0.10$), and then

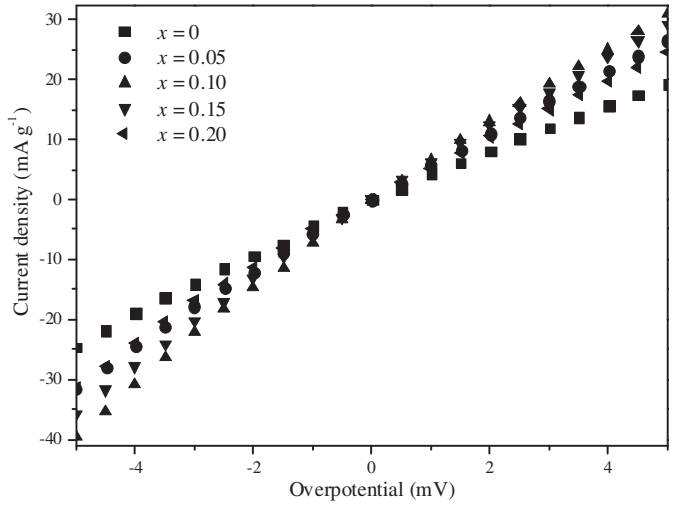

Fig. 7. Linear polarization of $La_{0.7}Ce_{0.3}Ni_{4.2}Mn_{0.9-x}Cu_{0.37}(Fe_{0.43}B_{0.57})_x$ alloy electrodes.

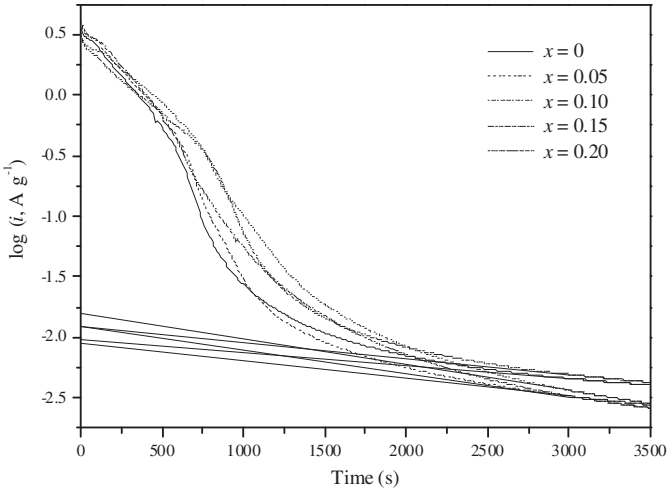

Fig. 8. Semilogarithmic curves of anodic current vs. time of response of $La_{0.7}Ce_{0.3}Ni_{4.2}Mn_{0.9-x}Cu_{0.37}(Fe_{0.43}B_{0.57})_x$ alloy electrodes.

decreases to 7.70×10^{-11} cm^2 s^{-1} ($x = 0.20$). Shu et al. [18] reported the formation of the secondary phase increases the fraction of phase boundaries, which provides extra tunnels for the diffusion of hydrogen atoms. The increase of $La_3Ni_{13}B_2$ secondary phase causes the increase in the phase boundary, which can decrease the lattice distortion and strain energy formed in the process of hydrogen absorption. Conversely, Khaldi et al. [35] have reported that the oxidation of Fe on the alloy surface limited the hydrogen transfer from the surface to the bulk. As mentioned above, the increase of Fe content causes the increase of surface oxide film, which will degrade the hydrogen diffusion. Therefore, it is certain that the diffusion coefficient has a maximum value with increasing x value.

4. Conclusions

On the basis of microstructures and electrochemical characteristics of $La_{0.7}Ce_{0.3}Ni_{4.2}Mn_{0.9-x}Cu_{0.37}(Fe_{0.43}B_{0.57})_x$ hydrogen storage alloys, the following conclusions can be drawn:

- Bimodal microstructures of $LaNi_5$ matrix and $La_3Ni_{13}B_2$ secondary phase are observed in $La_{0.7}Ce_{0.3}Ni_{4.2}Mn_{0.9-x}Cu_{0.37}(Fe_{0.43}B_{0.57})_x$ alloys with the substitution of Mn with $Fe_{0.43}B_{0.57}$. Moreover, the relative abundance of $La_3Ni_{13}B_2$ increases with the increment of x value.
- The activation performance is improved by substituting Mn with $Fe_{0.43}B_{0.57}$ alloy, which is ascribed to the increase in secondary phase and electrocatalytic activity of alloy surface.
- Maximum discharge capacity of the alloy electrodes decreases from 323.3 mAh g^{-1} ($x = 0$) to 311.3 mAh g^{-1} ($x = 0.20$). S_{100} monotonically decreases from 79.3% ($x = 0$) to 68.2% ($x = 0.20$), which is mostly affected by the degradation of corrosion resistance.
- HRD_{1200} first increases from 60.1% ($x = 0$) to 69.8% ($x = 0.10$), and then decreases to 63.2% ($x = 0.20$), which is determined by the exchange current density and hydrogen diffusion coefficient.

Acknowledgments

This research is financially supported by the National Natural Science Foundation of China (51001043), Program for New Century Excellent Talents in University (NCET-11-0943), China Postdoctoral Science Special Foundation (201104390), Program for Innovative Research Team (in Science and Technology) in the University of Henan Province (2012IRTSTHN007), Baotou Science and Technology Project (2011J1003) and the Doctoral Foundation of Henan Polytechnic University (B2010-13).

References

[1] T. Sakai, H. Yoshinaga, H. Migamura, N. Kurigama, H. Ishikawa, J. Alloys Compd. 180 (1992) 37–54.
[2] Y. Fukumoto, M. Miyamoto, M. Matsuoka, C. Iwakura, Electrochim. Acta 40 (1995) 845–848.
[3] X.D. Wei, P. Zhang, H. Dong, Y.N. Liu, J.W. Zhu, G. Yu, J. Alloys Compd. 458 (2008) 583–587.
[4] C. Iwakura, K. Ohkawa, H. Senoh, H. Inoue, Electrochim. Acta 46 (2001) 4383–4388.
[5] B. Zhang, W.Y. Wu, X. Bian, G.F. Tu, J. Alloys Compd. 538 (2012) 189–192.
[6] T.Z. Huang, Z. Wu, J.T. Han, G.X. Sun, J.M. Yu, X.Q. Cao, N.X. Xu, Y.H. Zhang, Int. J. Hydrogen Energy 35 (2010) 8592–8596.
[7] R. Tang, Y. Liu, C. Zhu, J. Zhu, G. Yu, Intermetallics 14 (2006) 361–366.
[8] K. Komori, O. Yamamoto, Y. Toyoguchi, K. Suzuki, S. Yamaguchi, A. Tanaka, M. Ikoma, US5512385, 1996.
[9] L. Jiang, G.X. Li, L.Q. Xu, W.Q. Jiang, Z.Q. Lan, J. Guo, Int. J. Hydrogen Energy 35 (2010) 204–209.
[10] D.L. Chao, C.L. Zhong, Z.W. Ma, F. Yang, Y.C. Wu, D. Zhu, C.L. Wu, Y.G. Chen, Int. J. Hydrogen Energy 37 (2012) 12375–12383.
[11] B.Z. Liu, A.M. Li, Y.P. Fan, M.J. Hu, B.Q. Zhang, Trans. Nonferrous Met. Soc. China 22 (2012) 2730–2735.
[12] S.Q. Yang, S.M. Han, Y. Li, S.X. Yang, L. Hu, Mater. Sci. Eng. B 176 (2010) 231–236.
[13] H. Ye, H. Zhang, W.Q. Wu, T.S. Huang, J. Alloys Compd. 312 (2000) 68–76.
[14] Y.H. Zhang, M.Y. Chen, X.L. Wang, G.Q. Wang, X.P. Dong, Y. Qi, Electrochim. Acta 49 (2004) 1161–1168.
[15] S.K. Pandey, A. Srivastava, O.N. Srivastava, Int. J. Hydrogen Energy 32 (2007) 2461–2465.
[16] M.B. Moussa, M. Abdellaoui, H. Mathlouthi, J. Lamloumi, A.P. Guegan, J. Alloys Compd. 458 (2008) 410–414.
[17] H. Ye, Y.X. Huang, J.X. Chen, H. Zhang, J. Power Sources 103 (2002) 293–299.
[18] Y.P. Fan, B.Z. Liu, B.Q. Zhang, L.Q. Ji, Y.G. Wang, Z. Zhang, Mater. Chem. Phys. 138 (2013) 803–809.
[19] B.Z. Liu, M.J. Hu, Y.P. Fan, L.Q. Ji, X.L. Zhu, A.M. Li, Electrochim. Acta 69 (2012) 384–388.
[20] B.Z. Liu, M.J. Hu, L.Q. Ji, Y.P. Fan, Y.G. Wang, Z. Zhang, A.M. Li, J. Alloys Compd. 516 (2012) 53–57.
[21] K.Y. Shu, S.K. Zhang, Y.Q. Lei, G.L. Lü, Q.D. Wang, Int. J. Hydrogen Energy 28 (2003) 1101–1105.
[22] W. Choi, K. Yamataka, S. Zhang, H. Inoue, C. Iwakura, J. Electrochem. Soc. 146 (1999) 46–48.
[23] D. Yan, G. Sandrock, S. Suda, J. Alloys Compd. 216 (1994) 237–242.
[24] M.S. Wu, H.R. Wu, Y.Y. Wang, C.C. Wan, J. Alloys Compd. 302 (2000) 248–257.
[25] H.Z. Yan, F.Q. Kong, W. Xiong, B.Q. Li, J. Li, L. Wang, Int. J. Hydrogen Energy 35 (2010) 5687–5692.
[26] T. Sakai, K. Oguro, H. Miyamura, N. Kuriyama, A. Kato, H. Ishikawa, J. Less-Common Met. 161 (1990) 193–202.
[27] D. Chartouni, F. Meli, A. Zuttel, K. Gross, L. Schlapbach, J. Alloys Compd. 241 (1996) 160–166.
[28] P. Li, X.L. Wang, Y.H. Zhang, R. Li, J.M. Wu, X.H. Qu, J. Alloys Compd. 353 (2003) 278–282.
[29] X.B. Zhang, D.Z. Sun, W.Y. Yin, Y.J. Chai, M.S. Zhao, Chem. Phys. Chem. 6 (2005) 520–525.
[30] P. Notten, P. Hokkeling, J. Electrochem. Soc. 138 (1991) 1877–1885.
[31] Y.F. Zhu, H.G. Pan, G.Y. Wang, M.X. Gao, J.X. Ma, C.P. Chen, Q.D. Wang, Int. J. Hydrogen Energy 26 (2001) 807–816.
[32] F. Meli, A. Zuttel, L. Schlabach, J. Alloys Compd. 202 (1993) 81–88.
[33] G. Zheng, B.N. Popov, R.E. White, J. Electrochem. Soc. 142 (1995) 2695–2698.
[34] B.Z. Liu, G.X. Fan, Y.C. Wang, G.F. Mi, Y.M. Wu, L.M. Wang, Int. J. Hydrogen Energy 33 (2008) 5801–5806.
[35] C. Khaldi, H. Mathlouthi, J. Lamloumi, A. Percheron-Guegan, J. Alloys Compd. 360 (2003) 266–271.